Article:
Zhang, H, Dickson, AN, Sheng, Y et al. (5 more authors) (2020) Failure analysis of 3D printed woven composite plates with holes under tensile and shear loading. Composites Part B: Engineering, 186. 107835. p. 107835. ISSN 1359-8368

https://doi.org/10.1016/j.compositesb.2020.107835

Failure analysis of 3D printed woven composite plates with holes under tensile and shear loading

Haoqi Zhang [1], Andrew N. Dickson [2], Yong Sheng [3], Terry McGrail [4], Denis P. Dowling [2], Chun Wang [5], Anne Neville [5], Dongmin Yang [1,*]

1. School of Civil Engineering, University of Leeds, Leeds, LS2 9JT, UK

2. School of Mechanical and Materials Engineering, University College Dublin, Ireland

3. Faculty of Engineering, University of Wolverhampton, Wolverhampton, WV1 1LY, UK

4. Irish Composite Centre (IComp), University of Limerick, Limerick, V35FT54, Ireland

5. Institute of Functional Surfaces, School of Mechanical Engineering, University of Leeds, Leeds, LS2 9JT, UK

Abstract

This paper presents the modelling and failure analysis of 3D printed woven composite plates with a hole under tensile and shear loading. In the finite element (FE) software, woven cells are built using stacking sequences, which are then linked together to form the FE model of the woven laminate. According to the 3D printing experiments, tailored fibre placement is achieved in the simulation by altering the fibre orientation around a region to leave a hole. In order to compare this placement technique with that of a control group, 'drilled' samples with the notch removed via mechanical machining was proposed. Three cases, open-hole laminates under tensile loading and double-shear and single-shear loading, are studied to advance the understanding of the failure mechanisms. Good agreement between numerical and experimental results has been obtained, which exhibits a similar trend of strength improvement using new placement technique. The distribution of principal strain and displacement in the modelling are consistent with the results obtained from Digital Image Correlation (DIC) and Micro X-ray Computed Tomography (Micro-CT). It suggests that the avoidance of fibre breakage and the overlap of printed materials around the hole can dramatically increase

* Corresponding author. Email: Dongmin.Yang@ed.ac.uk

the failure strength and prevent the propagation of cracks.

Keyword: Carbon fibre reinforced plastic (CFRP), 3D printing, Woven composites, Finite element analysis (FEA), Digital Image Correlation (DIC), Micro X-Ray computed tomography (Micro-CT).

1. Introduction

Additive manufacturing technology, commonly known as 3D printing, is a process that enables the efficient manufacturing of parts with complex shapes [1, 2]. At present, the most widely used 3D printing process is fused filament fabrication (FFF). From prototypes to final parts, automotive [3], aerospace [4], medical [5] industries have already adopted FFF as an alternative manufacturing process. FFF 3D printers use a thermoplastic filament, which is heated to its melting point and then extruded, layer by layer, to create a three dimensional object [6]. An emerging material for 3D printing is fibre-reinforced plastic (FRP), a composite material made of a polymer matrix reinforced with fibres, which is widely used for automotive and aerospace structures because of its high strength and high stiffness-to-weight ratio [7].

Recently, a few new 3D printing technologies for FRP composites have been developed. For example, Markforged released the first commercial system that could 3D print continuous fibre filament in 2014. The mechanical performance of composites with continuous fibre reinforcements including carbon, Kevlar and glass fibres has been evaluated by researchers [8-12]. The tensile strength value of printed composites reinforced by continuous carbon fibres is up to 6.3 times higher than that obtained with the non-reinforced nylon polymer [13]. Even the continuous aligned fibres can be printed along designed path, which offers more flexibility to overcome the major obstacle, the creation of assemblies from multiple components, in the area of composite manufacturing.

In traditional manufacturing, mechanical fastening (currently used for composite

joining) is required and notches have to be present in the structure before fastening, which creates major stress risers and weakens the composite material. For composite structures with geometric discontinuities, reinforced fibres are usually placed straight in each layer and the notch punching process would cut off those fibre, which underutilises the outstanding properties of them. Some optimal designs of continuous fibre placement have been made for the 3D printed FRP composites to fully utilise the properties of the fibre [14-17], typically follow a path for fibre determined by finite element models [18-20].

Tailored fibre placement or fibre steering is a technique for placing fibres by using a sewing or tape placement system, which has been used to increase the mechanical performance of composite materials. Some researchers applied this idea to 3D printing to solve the joining problem. They introduced a new fibre placement technique, which allows for the printing of woven multi-laminate composite structures with complex internal geometries [21, 22]. The results were then compared with that of similar composites processed through current state-of-art machining processes, which showed it has the potential as a replacement technology for joining or repairing composites. But there was limited experimental data available from the fracture processes so further analysis especially for internal material information and crack propagation needs to be conducted to evaluate the failure mechanism of these woven multi-laminate composite structures.

In this paper, 3D printed woven carbon fibre reinforced plastic (CFRP) composites were investigated by finite element analysis (FEA) to explore the failure mechanisms of 3D printed woven composites. Firstly, the new fibre deposition technique and the numerical simulation method are presented. Then open hole tensile and shear bearing response tests are carried out by the finite element method. The numerical results are discussed and compared with the experimental results, in order to identify the reasons why 3D printed woven multi-laminate composite structures have better performance. Also the Digital Image Correlation (DIC) and Micro X-ray computed tomography (Micro-CT) scanning were used to characterize the specimens to obtain more analytical

information about failure. From the correlation between FEA, DIC and micro-CT data, damage evolution processes under tensile and shear loading conditions were revealed.

2. 3D printing of woven composites

2.1 3D Printing System & Materials

The carbon fibre feedstock filament was sourced from Markforged CA. These filaments (0.35mm diameter) consist of two materials, a fibre bundle (reinforcement) and an impregnated polymer (matrix). The fibre bundle consists of approximately 1000 continuous 7μm diameter carbon fibres. The matrix material is a Nylon blend developed by Markforged. The filament is provided on 150cm^3 or 50cm^3 spools and is stored in a dry box to reduce moisture uptake, this is due to Nylons hygroscopic nature. The thermal properties of the "prepreg" carbon fibre filaments are evaluated using differential scanning calorimetry (DSC). The glass transition temperatures T_g = 68 °C but the melting peak was found to be absent even the filaments was exposed to 250°C for 30 hours [23]. Previous authors have highlighted that the shape and size of the melting peaks observed in DSC are dependent on the thermal history of the nylon polymer [24]. This indicates that the filament may have been exposed to relatively high temperature during the fabrication process.

Printing was carried out utilising a Prusa i3 printer chassis with a modified fibre printing head. A 1.3mm Markforged fibre nozzle was installed. For the specimen produced in this study a print temperature of 245°C, and a speed of 10mm/s was used. Samples were printed onto an unheated Garolite print plate which was coated in a layer of PVA, to ensure adequate adhesion during printing.

2.2 Fibre pathing

The filaments used in this study contains continuous fibres, and as such toolpaths cannot stop and start as they would during polymer printing. It was therefore necessary to generate a continuous toolpath (G-code), as described previously [21]. Continuous

toolpaths were generated through a parametric Python script, with output commands compiled in a spreadsheet software package before transfer to the printer. Sample plates could be customised by the altering input parameters (such as sample size, weave spacing, feature locations, print speed, etc.). Examples of rectangular woven laminates are shown in Fig. 1. Note that carbon fibre stiffness precludes the use of tight cornering whilst printing. It was therefore necessary to take larger sweeping corners to avoid fibre breakages, which caused 'selvedge' (excess) material in the preparation of specimens. It can also be seen in Fig. 1 how different numbers of filaments within each unit cell affect the woven structure. This can also drastically reduce the 'selvedge' material, as seen when comparing that of the tensile and the bearing response specimen patterns. The path used in the bearing response specimen was more efficient with less wastage.

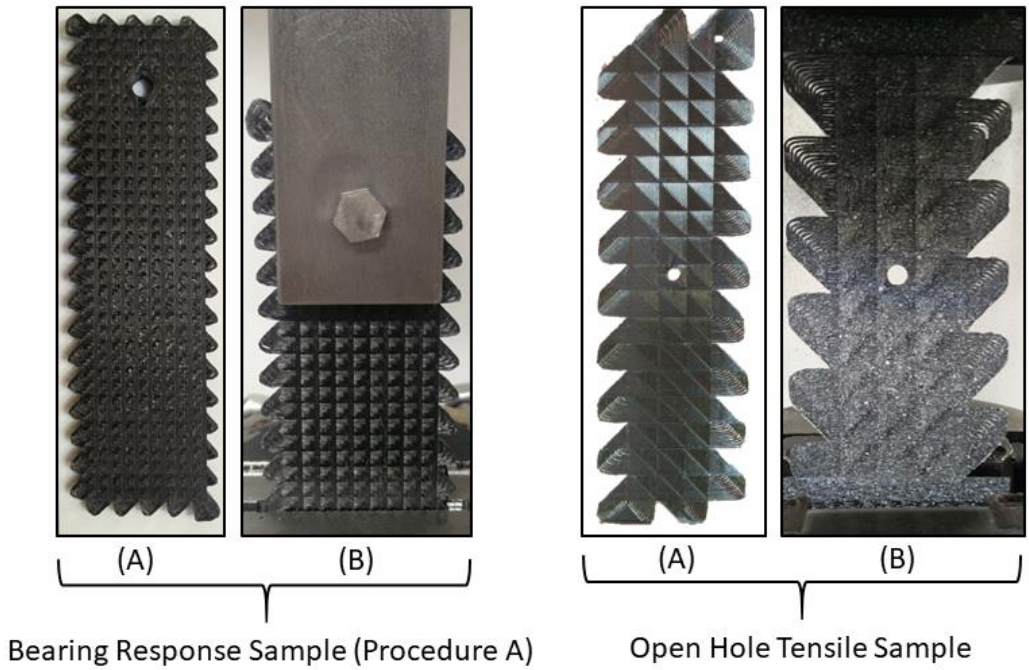

Fig. 1 Finished composite sample (A) and sample mounted (B) for both open hole tensile and bearing response tests. A smaller woven unit cell was used to minimize waste material in bearing response samples.

2.3 Tailor woven and drilled samples

In order to compare this tailored placement technique with that of a baseline/control group, a second group of samples was proposed. These 'drilled' samples had a 6mm

notch removed from the required locations via mechanical machining. In the case of open-hole tensile samples this was achieved through die punching the samples, which was possible due to their low thickness of just 0.35mm. As bearing samples were approximately 3.1mm thick it was necessary to drill the notches using a diamond coated bit. An example of both a 'tailor woven' and a 'drilled' 6mm notch are shown in Fig. 2.

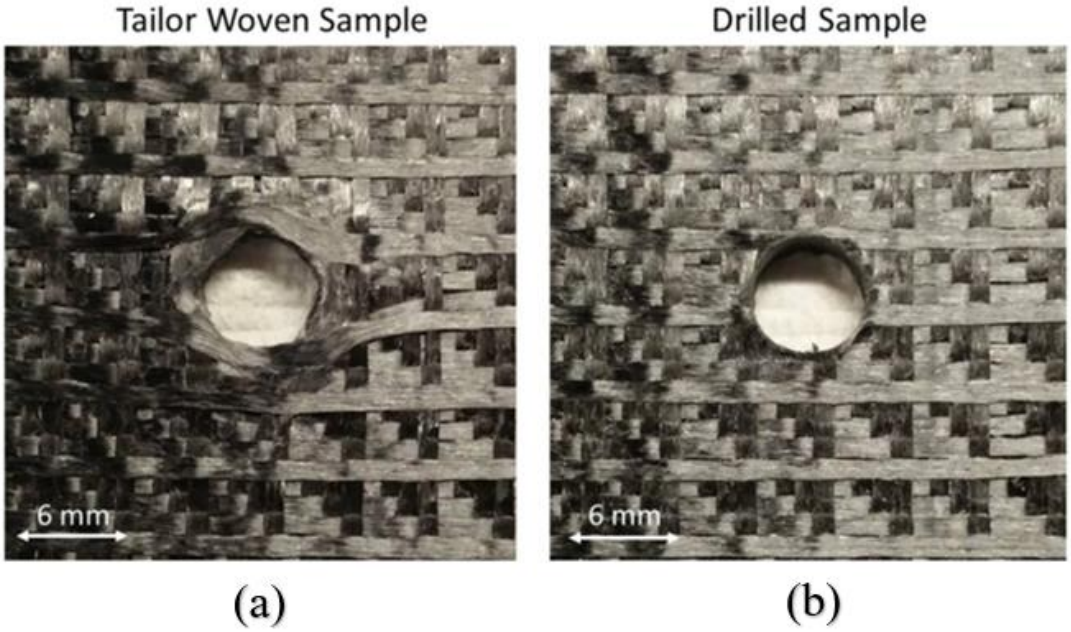

Fig. 2 The 'tailor woven' (a) and 'drilled' (b) samples for bearing response testing. Note the fibres remain unbroken in the 'tailor woven' samples versus the discontinued fibres in the 'drilled' sample

2.4 Mechanical testing

This section introduces the specimen setup in the experiment. Detailed geometric information and schematic diagram will be shown in next section. Both open hole tensile and bearing response tests were performed on an Instron 100kN 8501 hydraulic tester (50kN in Tensile). Hydraulic grips ensure equal gripping pressure on each tab (500Psi). A preload of 5N was applied to specimen prior to test start to take up slack from gripping apparatus.

As per ASTM D5766 (open hole tensile) the specimens were tested at a crosshead speed of 1mm/min. And they were adhesively bonded onto carbon epoxy tabs, this acts

to minimise strain concentrations at the gripping points, and was particularly important for un-notched samples which contained no hole for strain concentration.

As per the ASTM D5961 (bearing response) standard the specimens were tested at a crosshead speed of 2mm/minute. Double shear specimens were held in a steel support structure using a steel M6 nut and bolt, tightened to a torque of 3Nm (using a Torqueleader ADS 4, 0.8-4Nm, torque wrench). This structure evenly applies shear from either side of the specimen. In the case of single shear specimen, carbon epoxy doublers were bonded to the ends of each specimen using a toughened cyanoacrylate to reduce stress concentrations from the grips. A steel M6 nut and bolt were then used to fasten the two specimens together with an applied torque of 3Nm. Two M6 washers were also used as pressure distributors on either side.

2.5 Digital Image Correlation (DIC) and computed tomography (CT) scanning

Digital image correlation system was used as a video extensometer to obtain extension measurement. Since the bolts in the shear loading tests covered the hole, this system was only used for the specimens in open-hole tensile test. A crosshead speed of 1mm/min was used so as to acquire accurate DIC readings. For this detection system to function, a random speckle pattern was applied to the surface of the specimens. A white elastic spray paint was used to speckle this pattern.

The specimens after failure in shear loading tests were examined by a Zeiss Xradia Versa 410 Micro-CT system. The same micro-CT parameters were used for specimens in double and single shear loading tests and produced a voxel size of 1.9397μm. An accelerating voltage of 80keV and a power of 7W were used in this system. The specimens were rotated 360° and 1600 projections at one second exposure time were collected on a charge-coupled device detector. To obtain clear images, results from Micro-CT system were reconstructed using Zeiss built-in reconstruction software and the threshold value was determined by analysing experience.

3. Failure characterization and finite element analysis

3.1 Finite element model

In this paper, a FEM software ABAQUS is used to simulate the failure of 3D printed woven composites plates. The plates are set as 3D shell models and the 'composites layup' module is applied to define the stacking sequence and properties of the elements. The elastic properties and damage properties of CFRP used in the present study are shown in Table 1 and Table 2 respectively. The damage initiation and evolution of fibre reinforced composites are judged by using Hashin failure criteria in ABAQUS, which is based on the works of Hashin and Rotem [25].

Four different damage initiation mechanisms are taken into consideration in the Hashin damage initiation criterion: fibre tension (F_f^t), fibre compression (F_f^c), matrix tension (F_m^t), and matrix compression (F_m^c). According to the failure modes, the following four equations Eqs (1) - (4) are applied.

$$F_f^t = \left(\frac{\sigma_{11}}{X^T}\right)^2 + \alpha\left(\frac{\tau_{12}}{S^L}\right)^2 \quad (1)$$

$$F_f^c = \left(\frac{\sigma_{11}}{X^C}\right)^2 \quad (2)$$

$$F_m^t = \left(\frac{\sigma_{22}}{Y^T}\right)^2 + \left(\frac{\tau_{12}}{S^L}\right)^2 \quad (3)$$

$$F_m^c = \left(\frac{\sigma_{22}}{2S^T}\right)^2 + \left[\left(\frac{Y^C}{2S^T}\right)^2 - 1\right]\frac{\sigma_{22}}{Y^C} + \left(\frac{\tau_{12}}{S^L}\right)^2 \quad (4)$$

where σ_{11}, σ_{22} and τ_{12}, are the applied stresses and α is a coefficient ($0.0 \leq \alpha \leq 1.0$) that determines the contribution of the shear stress to the fibre tensile initiation criterion. In this work, the value α =1.0 is used as in the model proposed by Hashin in 1980 [26].

In ABAQUS software, the Hashin criterion is parallel to the evolution of damage. It is based on four fracture energies which correspond to four different material failure modes. The fracture energy values presented in Table 2 was used for each mode previously explained. However, it is a challenge that using damage energy to determine the combination of Hashin criterion and damage evolution. Other standard tests on

fracture energies of FRP composite are still to be developed [27-29].

When one of the parameters (F_f^t, F_f^c, F_m^t and F_m^c) exceeds the unit value, the damage criterion of the corresponding failure mode is met, and the stress at this point is calculated as follows:

$$\sigma = C_d \varepsilon \tag{5}$$

where ε reflects the strain and C_d reflects the matrix of damaged elasticity:

$$C_d = \frac{1}{D}\begin{bmatrix} (1-d_f)E_1 & (1-d_f)(1-d_m)v_{21}E_1 & 0 \\ (1-d_f)(1-d_m)v_{12}E_2 & (1-d_m)E_2 & 0 \\ 0 & 0 & (1-d_s)GD \end{bmatrix} \tag{6}$$

$$D = 1-(1-d_f)(1-d_m)v_{12}v_{21} \tag{7}$$

where E_1, E_2, G, v_{12} and v_{21} are shown as Table 1. And d_f, d_m and d_s reflect the current state of fibre, matrix and shear damage respectively, which derived from damage variables d_f^t, d_f^c, d_m^t and d_m^c as follows:

$$d_f = \begin{cases} d_f^t & \text{if } \sigma_{11} \geq 0 \\ d_f^c & \text{if } \sigma_{11} < 0 \end{cases} \tag{8}$$

$$d_m = \begin{cases} d_m^t & \text{if } \sigma_{22} \geq 0 \\ d_m^c & \text{if } \sigma_{22} < 0 \end{cases} \tag{9}$$

$$d_s = 1-(1-d_f^t)(1-d_f^c)(1-d_m^t)(1-d_m^c) \tag{10}$$

After the damage initiates, the damage variable of each mode is calculated by means of

$$d = \frac{\delta_{eq}^f(\delta_{eq}-\delta_{eq}^0)}{\delta_{eq}(\delta_{eq}^f-\delta_{eq}^0)} \tag{11}$$

where δ_{eq}^0 is the equivalent displacement when the damage criterion of material was met initially and δ_{eq}^f is the equivalent displacement when the material was damaged completely. Fig. 3 shows their relation graphically. The values of δ_{eq}^0 for the various

modes depend on the elastic stiffness and the strength parameters specified as part of the damage initiation definition. The values of δ_{eq}^{f} for the various modes depend on the respective energy dissipated during damage G^{c}.

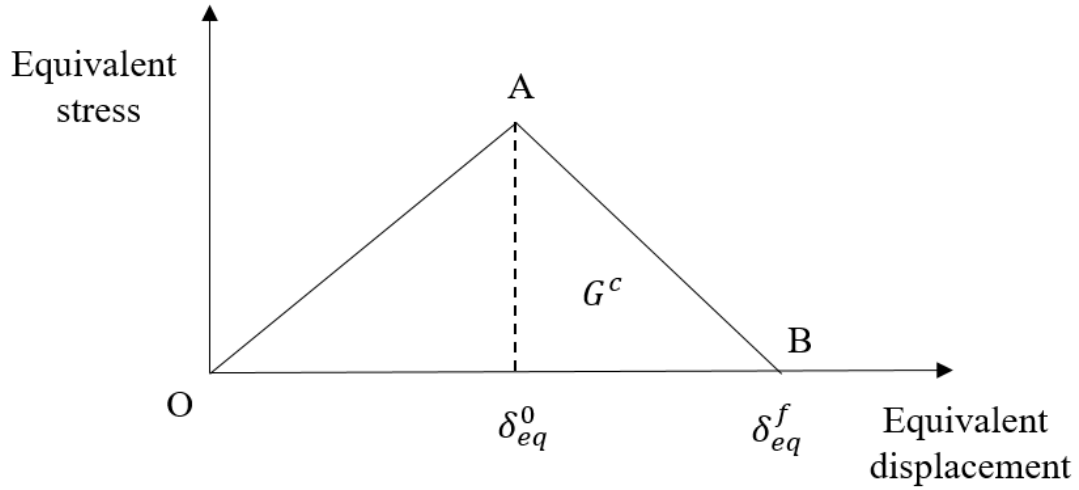

Fig. 3 Linear damage evolution of Hashin failure criteria.

Table 1 Elastic properties of 3D printed CFRP by Mark One/Two [12, 30].

Modulus of elasticity in fibre direction ($\mathbf{E_1}$)	54 GPa
Modulus of elasticity in transverse to fibre direction ($\mathbf{E_2}$)	26 GPa
In plane Poisson's ratio ($\mathbf{v_{12}}$ & $\mathbf{v_{21}}$)	0.30
Share modulus ($\mathbf{G}$)	5000 MPa

Table 2 Damage properties of 3D printed CFRP by Mark One/Two [12, 31, 32].

Tensile strength in carbon fibre direction ($\mathbf{X^T}$)	700 MPa
Compressive strength in carbon fibre direction ($\mathbf{X^C}$)	320 MPa
Tensile strength in transverse to carbon fibre direction ($\mathbf{Y^T}$)	33 MPa
Compressive strength in transverse to carbon fibre direction ($\mathbf{Y^C}$)	131 MPa
Longitudinal shearing strength ($\mathbf{S^L}$)	29 MPa
Transverse shearing strength ($\mathbf{S^T}$)	29MPa
Tensile fracture energy in carbon fibre direction ($\mathbf{G_{ft}^c}$)	91.6 N/mm
Compressive fracture energy in carbon fibre direction ($\mathbf{G_{fc}^c}$)	79.9 N/mm
Tensile fracture energy in transverse to carbon fibre direction ($\mathbf{G_{mt}^c}$)	0.22 N/mm
Compressive fracture energy in transverse to carbon fibre direction ($\mathbf{G_{mc}^c}$)	1.1 N/mm
Viscosity coefficient	0.005

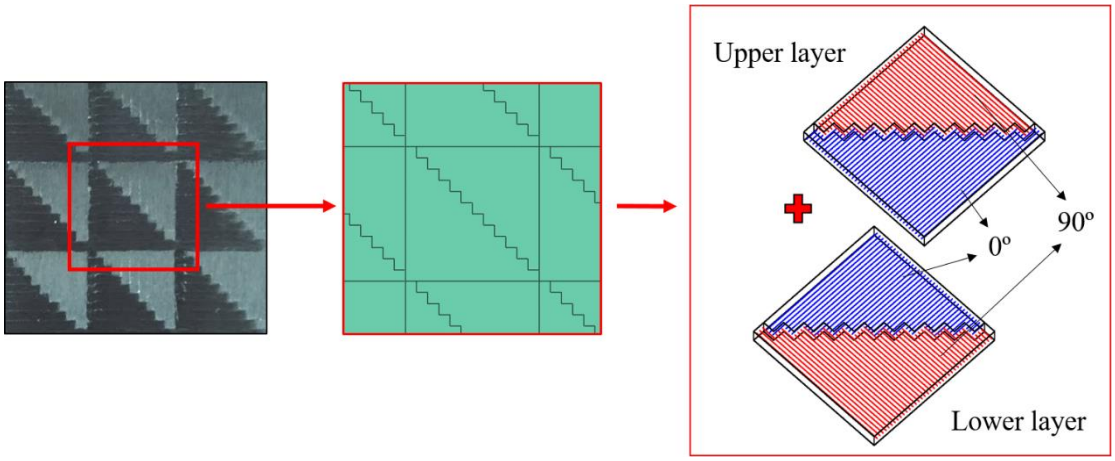

Fig. 4 Modelling of woven composites structure: detailed image of finished woven laminate (left), 'cell' structure in FEA (middle) and schematic representation of a two-layers woven cell (right).

The woven structure produced in this study can be broken down into unit cells (Fig. 4 highlights nine of these 'cells'). The modelling of woven laminate begins with the simulation of these square cells, as shown in Fig. 4. Each cell consists of two parts which are separated by polylines from topleft to downright. For a two-layer woven laminate, the stacking sequences of fibres are exactly the opposite in these two parts, $(0/90)_s$ and $(90/0)_s$ respectively. This modelling method makes the material properties of the woven composites in the numerical simulation similar to the experimental ones.

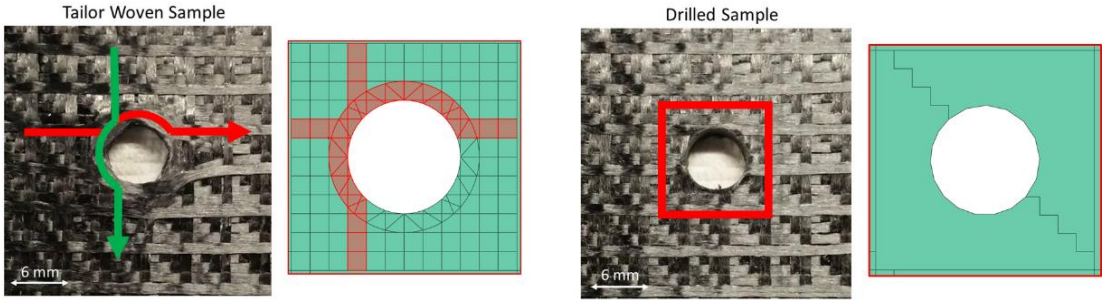

Fig. 5 Modelling of the hole for (a) 'Tailor-woven' and (b) 'drilled' specimens

As shown in Fig. 5 (a), fibres from the X and Y axis were diverted around a region to leave a hole in the 'tailor woven' specimen. In the real printed samples, the overlap of the filaments would cause the ring area to swell slightly and form a densified buffer zone. In the FE model, a ring with the same width as printing width (1mm) is set around

the hole. The first material orientation (fibre direction) of CFRP is set along this ring when the printing paths of the filament get into this ring region. Since the diameter of the hole is 6 mm, six printed filaments were diverted in the X and Y axis directions, in which the overlap of materials is formed as the overlap of red and green lines shown in Fig. 5(a). It causes different height in the ring and other regions and also improves the stiffness in the region around the hole, which is consistent with the case of real printed samples.

For the 'drilled' specimen, specimens are notched using a die punch after printing. In numerical simulations, a model of intact woven composites without holes is made firstly and a hole is cut off from the centre of the intact model to form the drilled case, as shown in Fig. 5 (b).

3.2 Tensile loading test

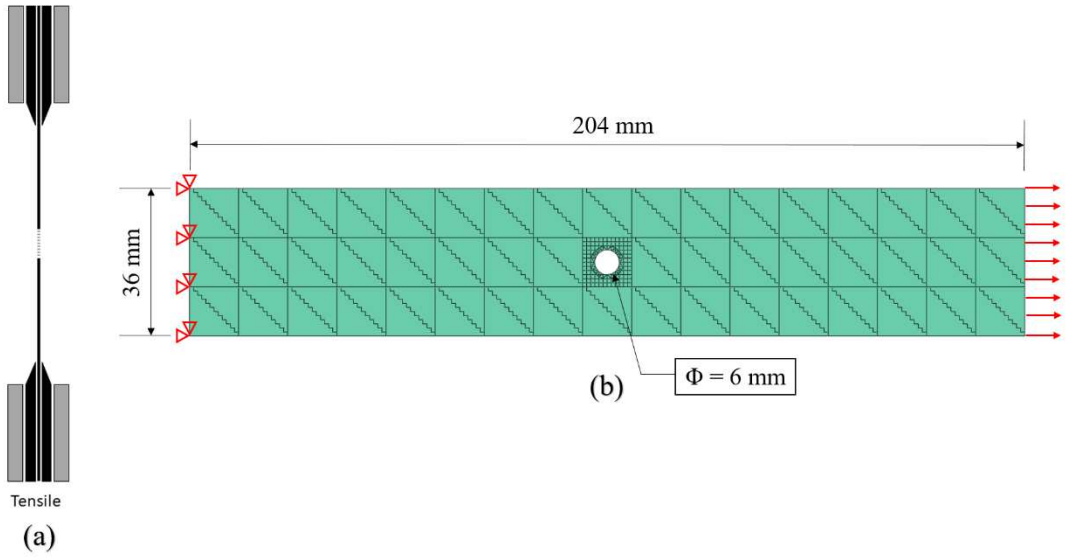

Fig. 6 (a) Specimen setup for tensile test (b) the schematic diagram in the FE model

As shown in Fig. 6, the first case is an open-hole laminate under uniaxial tensile loading according to ASTM-D5766 standard test method, where its length is 204 mm and its width is 36 mm. As mentioned above, a hole with 6mm diameter is placed in the centre and the plate consists of 2 plies of 0.17 mm thick. Each two plies make up a woven layer. The left side of the plate is fixed and the displacement along longitudinal

direction is applied to the right side of the plate. The plate has a constrained degree of freedom in vertical displacement along the z-axis to eliminate the effect of warpage on the results. ‘Tailor woven’, ‘drilled’ and ‘intact’ specimens are studied in this case.

3.3 Shear loading test

Numerical simulations of shearing tests were carried out according to ASTM-D5961 standard test method. These two cases are the laminates under double and single shear loading, where their length is 172 mm and their width is 36 mm. The plates consist of 18 plies of 0.175 mm thick (9 woven layers) and the dimeter of the holes is 6mm. According to standard test method for shearing response, the centre of the hole is 20 mm from the right side and 18 mm from the top side. For double shear loading test, the left side of the plate is fixed and a rigid pin is placed in the hole with the same diameter and the displacement along longitudinal direction, as shown in Fig. 7. For single shear loading test, the rigid pin is bound to a bolt of 2 mm thick and 6.5 mm in diameter. As shown in Fig. 8, displacement of pin is loaded in the position 1.575 mm (half of the plate thickness) from the plate, which ensures the woven laminates are under the same loading condition as in the experiment. In the simulation of shearing tests, the plates have a constrained degree of freedom in vertical displacement along the z-axis in order to eliminate the effect of warpage caused by the unsymmetrical stacking sequence of real samples. And the default set of contact is used in the interaction between the pin and the woven composites, which is ‘frictionless’ and ‘hard contact’ (only allow the transfer of compressive stress) for tangential and normal behaviour. Only ‘tailor woven’ and ‘drilled’ specimens are studied in shear loading tests.

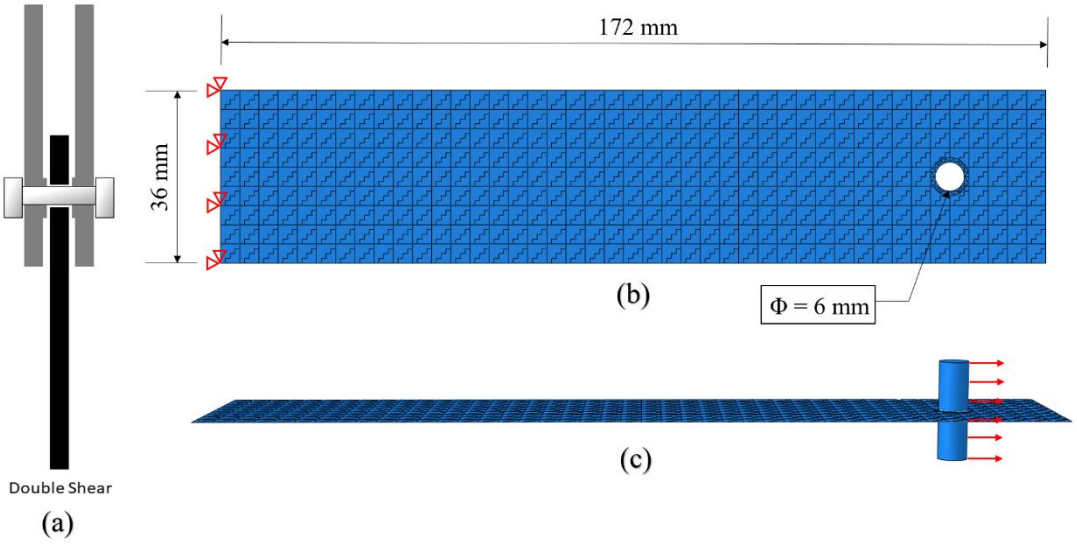

Fig. 7 Specimen setup (a) for double shear loading test and the schematic diagram from top view (b) and front view (c) in the FE model

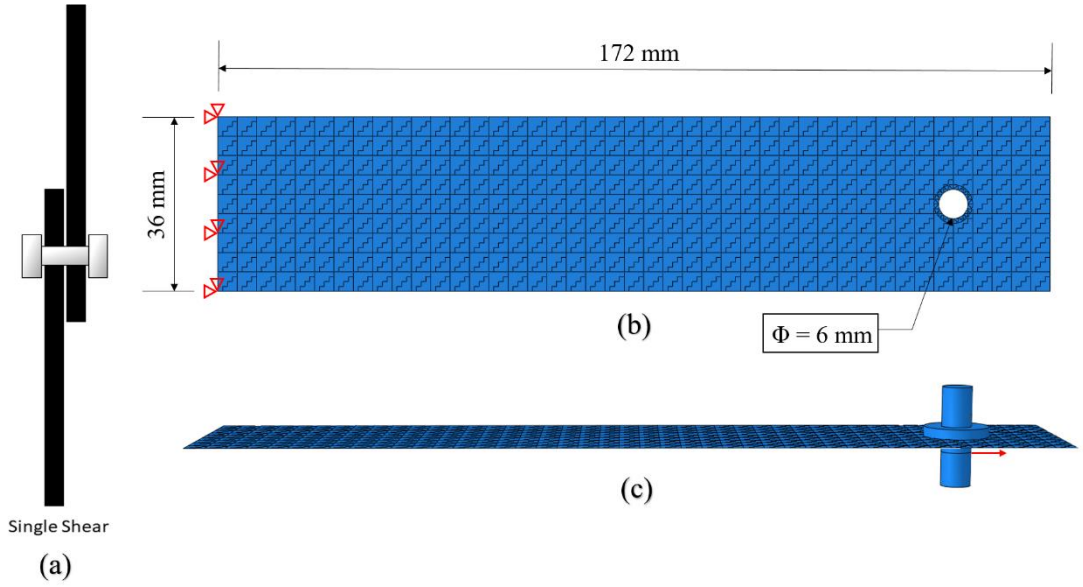

Fig. 8 Specimen setup (a) for single shear loading test and the schematic diagram from top view (b) and front view (c) in the FE model

4. Results and discussion

In this section, the results of the numerical simulations are compared with that obtained from the experimental data which were reported previously [21]. Just to note that there is limited experimental data available from the fracture processes, as these are hard to observe during the tensile and shearing tests.

4.1 Open hole tensile

In the tensile loading case, examples of the average tensile strengths and strains for each specimen are shown in Fig. 9 and stress-strain graphs compiled in Fig. 10. For ‘tailor woven’ and ‘intact’ specimens, the tensile strength from numerical simulations are 10-15% higher than those obtained experimentally. A possible explanation for this behaviour is that the presence of air voids caused by 3D printing process would reduce the material properties of CFRP and make the strength values a little lower than the materials data provided by Markforged company [30] while approximately 60% higher for ‘drilled’ specimen resulted in a considerable number of defects in the region around the hole such as fibre breakage, which could not be directly simulated in the present FE model. Comparing the experimental and modelling data given in Fig. 9 & Fig. 10, it is clear that both exhibit a similar trend of strength improvement obtained for the hole obtained using the ‘tailor woven’, compared with that for the drilling technique. In the presented FEA results, the strength of ‘drilled’ specimen reach 76% that of intact specimen, while ‘tailor woven’ specimens exhibited strengths which were 11% higher, and 13% lower than that of ‘intact’ specimens. Fig. 9 also shows the comparison of tensile strains for ‘tailor woven’, ‘drilled’ and ‘intact’ specimens (1.4%, 1.3% and 1.7% respectively in the simulation). The tensile strains of ‘tailor woven’ and ‘intact’ specimens show good agreement between the experiment and simulation while the value of ‘drilled’ specimen in the experiment is lower than that in simulation. As mentioned before, this is because in reality the drilling process of CFRP composites cuts off the carbon fibres and also generates serious defects including burrs, tearing, delamination, matrix thermal damage and so on [33]. These defects reduced the properties of the material around the hole and lowered the experimental strength of the ‘drilled’ sample.

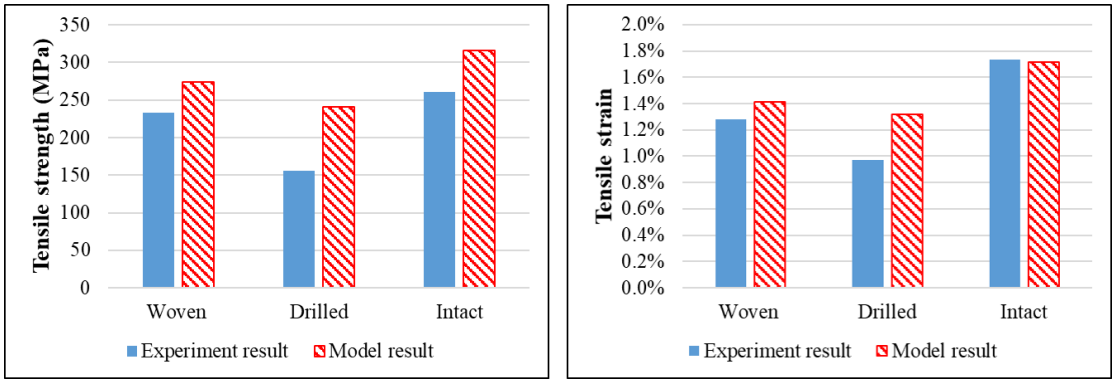

Fig. 9 Tensile strength (left) and tensile strain (right) for each type of specimen

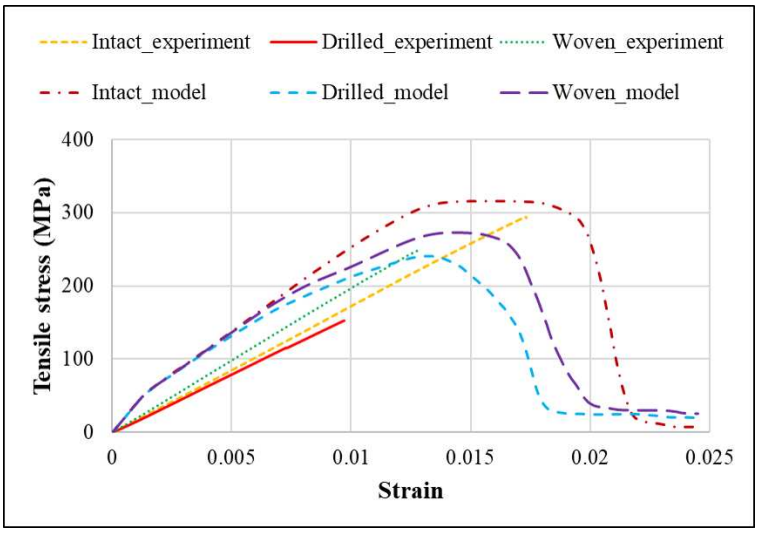

Fig. 10 Stress-strain curve for each type of specimen in tensile loading tests

As shown in Fig. 11, the maximum principal strain distribution from the FEA is similar to that in DIC images, which illustrates the reliability of the FE models. For the 'drilled' specimen, the immediate left and right regions of the hole bear most of the load due to the discontinuity of the fibres caused by the die punching process. As shown in Fig. 11(b) & (c), the strains with higher values (in red colour) concentrate in very small regions in the vicinity of the hole and the cracks propagate straight along the left and right directions. The failure mode was consistent with the type LGM (lateral, gage and middle) failure in ASTM D5766, wherein the laminate failed in tension laterally across the centre of the hole and exhibited faster crack propagation. For the 'tailor woven' specimen, maximum principal strains still concentrate around the hole but not in the immediate left and right regions since more materials are placed in this area during the 3D printing woven process. These continuous and uncut fibres transferred and

distributed the loads from the hole to the surrounding area, which makes it like a variable-stiffness design [34] where the material orientations are allowed to vary in a continuous manner over the domain. As similar optimization of fibre orientations near a hole [14, 35], tailor woven technique did reduce the localised strains and increase load-carrying capacity. Instead strains are concentrated on the corners of the region around the hole, which can be seen in the FEA contours as well for the level of strain given in the DIC images. It was observed that cracks initiated from the corners and then propagated outwards in a more irregular pattern compared with that obtained for the drilled composite, as shown in Fig. 11. The failure mode is the type MGM (multi-mode, gage and middle), in which laminate failed in tension at the hole and exhibited multiple modes including laterally and angularly in various sub-laminates. Also crack arrest was observed at weft-warp intersections, shifting the crack onto a different layer, as shown in Fig. 11(a).

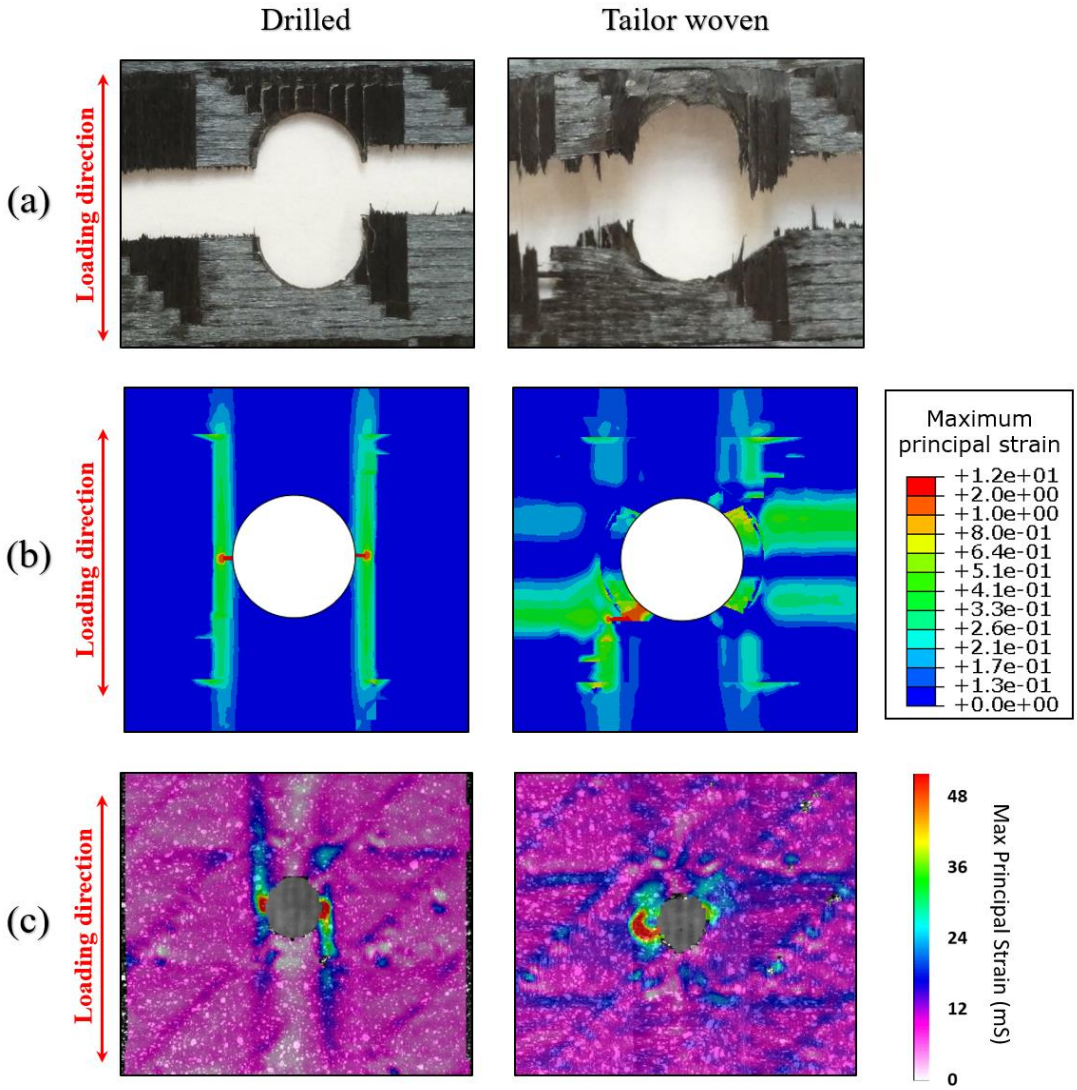

Fig. 11 Fracture pattern of 'drilled' (left) and 'tailor woven' (right) specimens: (a) fracture zone around the hole in experiment, (b) the distribution of maximum principal strain from FEA prior to failure and (c) DIC images immediately prior to failure.

4.2 Double Shear Bearing Response

The average shear strengths and strains for 'tailor woven' and 'drilled' specimens in double shear loading test are compiled in Fig. 12. Good agreement between numerical and experimental results has been obtained, where the shear strength increases from about 150 MPa to 250 MPa for the holes obtained using the tailor woven placement, compared with the drilled composites. The shear strains of 'tailor woven' specimen are similar but there are some differences of the shear strains of 'drilled'

specimen. As the stress-strain graphs shown in Fig. 13, when the strain reached to 22%, the curves of 'drilled' specimens come to the inflection point, which means the damage starts to develop in the laminate. However, in the experimental result, bearing stress continues to increase by about 20% as the stiffness declines. Since the actual printed materials contain lots of voids, the material around the hole shifted as it was squeezed by the steel pin, which can be observed in the Mirco-CT images below. For FEA results, the failure progress evolved more quickly because the material is assumed to be ideal and homogeneous in the simulation.

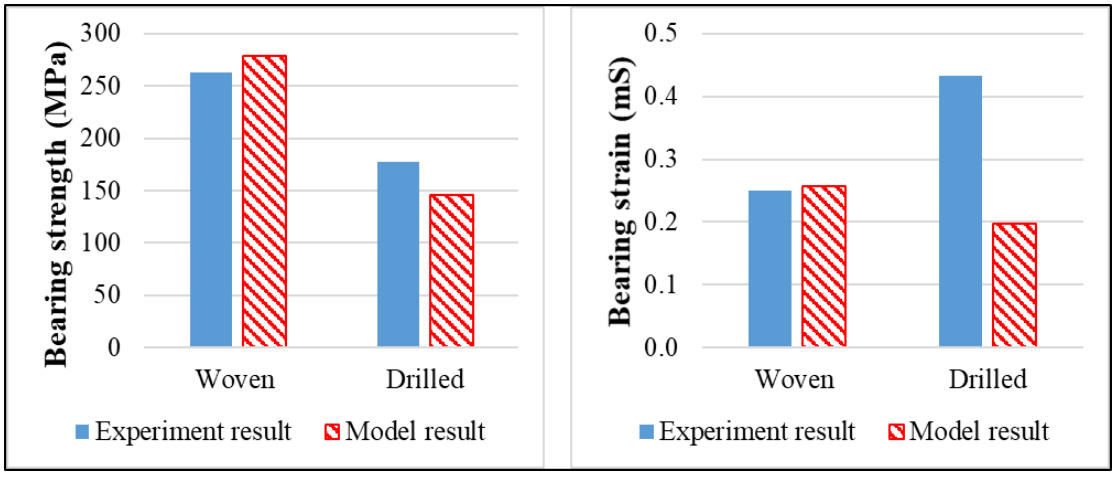

Fig. 12 Bearing strength (left) and strain (right) for 'tailor woven' and 'drilled' specimens in double shear loading test

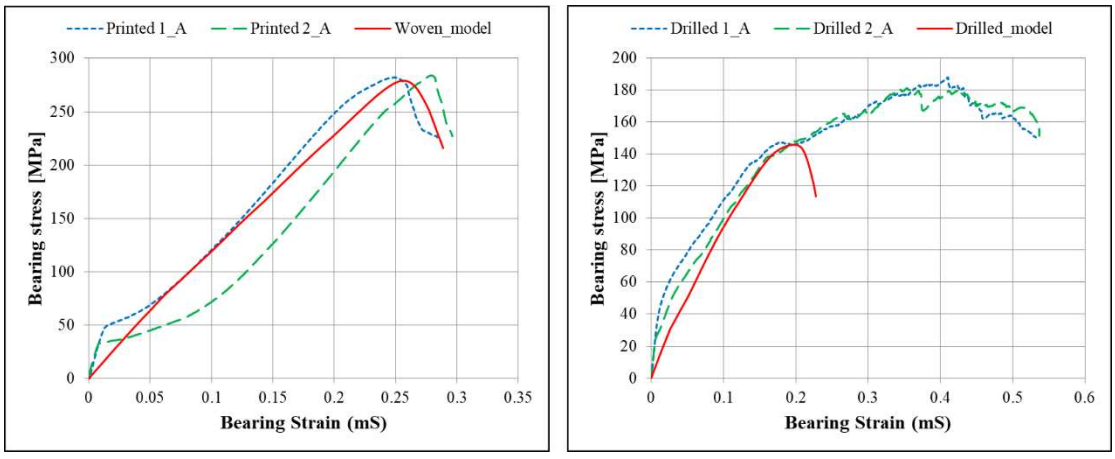

Fig. 13 Stress-Strain Curves for 'tailor woven' (left) and 'drilled' (right) specimens in double shear loading test

The progressive distributions of maximum principal strain are shown in Fig. 14,

which indicate how the damage initiates and propagates in the plate. For the ‘drilled’ specimen, the cracks initiate on the flanking sides of the hole and then propagate along the longitudinal direction, which is consistent with the 'shearout' failure mode. Instead the damage of ‘tailor woven’ specimen only occurs at the edge extruded by the steel pin and do not propagate to other areas of the plate. It is the B1I (bearing, first hole and inapplicable) failure mode in ASTM D5961. CT scan images shown in the Fig. 15(a) confirm the FEA results discussed above. The cracks are marked by the red circles, which show the damage actually occur at the flanking sides in the ‘drilled’ specimen and at the edge extruded by the steel pin in the ‘tailor woven’ specimen. Also, the deformed shapes of the hole are similar between the experimental and numerical results in Fig. 15(a) & (b), where the hole has undergone a huge deformation in the ‘drilled’ specimen because of the extrusion of the pin. Some fibre displacement is also visible at the hole of ‘tailor woven’ specimen, but this elongation is minor compared to that observed in the case of the drilled specimen. Fig. 15(c) shows that the improvement of shearing strength and difference of failure process are caused by the overlap of continuous materials around the hole in the ‘tailor woven’ specimen. The diversion of the filament around the hole makes the material dense in this region, which protects the specimen from the damage and crack propagation. In contrast, major buckling and delamination are seen in drilled specimens, as a result of compression of the discontinued fibres.

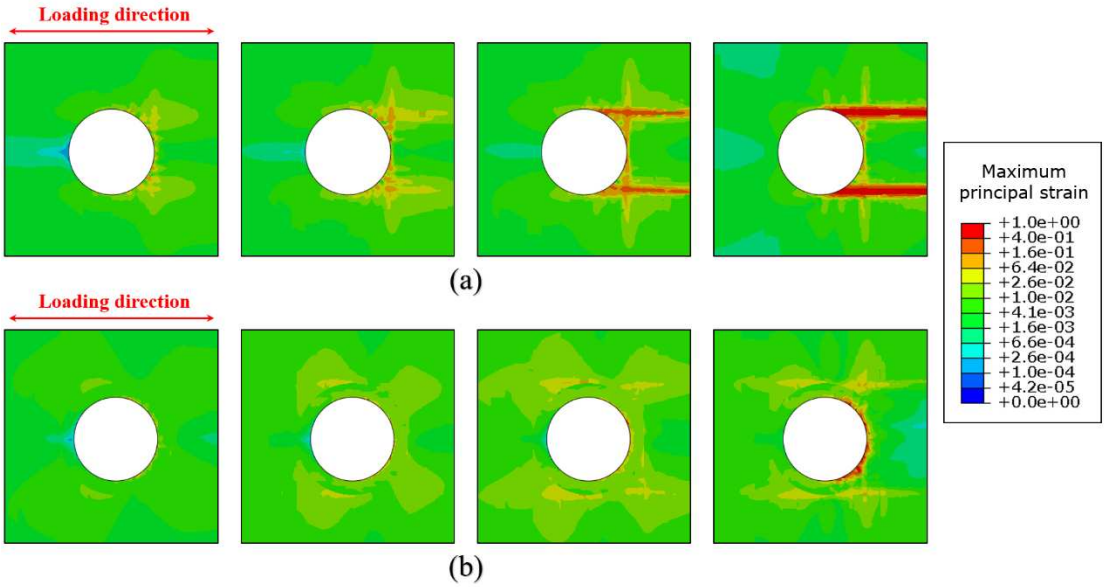

Fig. 14 The progressive distributions of maximum principal strain in double shear loading test: (a) ‘drilled’ and (b) ‘tailor woven’ specimens.

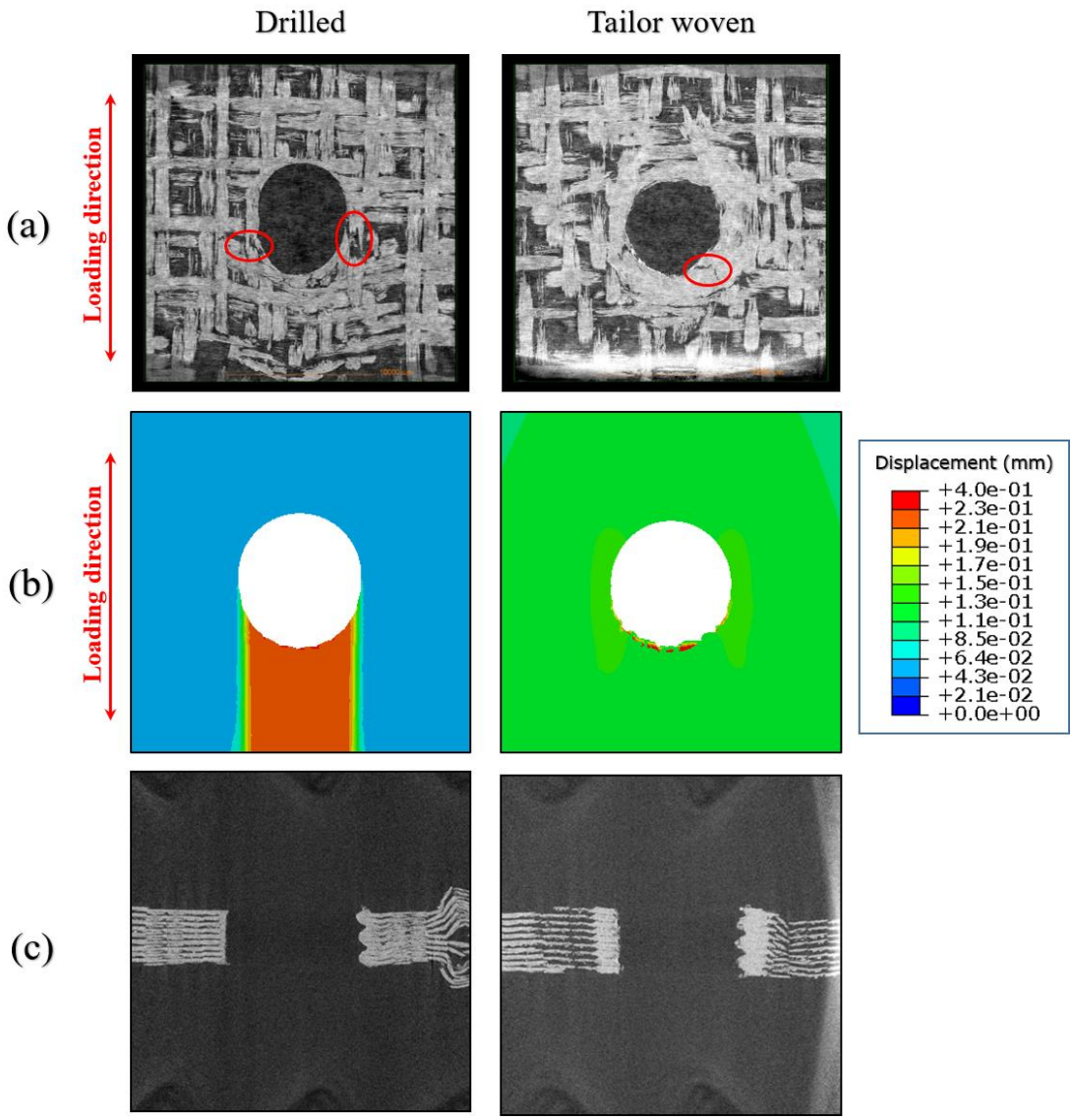

Fig. 15 Integrity of the hole after double shear loading test, 'drilled' specimen (left) and 'tailor woven' specimen (right): (a) Cross section images after failure from Micro-CT scanning, (b) Distribution of displacement after failure from FEA and (c) vertical section images after failure from Micro-CT scanning.

4.3 Single shear bearing response

The average shear strengths and strains for 'tailor woven' and 'drilled' specimens in single shear loading test also show good agreement, as shown in Fig. 16. Shear strength increases from about 150 MPa to 200 MPa and the comparison of stress-strain graphs shown in Fig. 17 is similar to those graphs in double shear loading test. In general, except for the different shear strength due to loading conditions, the damage processes of these two shear loading tests are similar and the mechanisms behind them

are the same. Another difference is the compression caused by bolt rotation in single shear loading. In term of it, tailor woven specimen exhibited better resistance and reduced the movement of the bolt. In contract, buckling due to the compression from the bolt is observed in the drilled specimen, and therefore delamination occurs above the hole. The distributions of maximum principal strain in Fig. 18 indicate the cracks initiate at the flanking sides of the hole in the 'drilled' specimen. And the damage in 'tailor woven' specimen only concentrate on the edge extruded by the steel pin, which also can be seen from the Micro-CT images in Fig. 19(a). So the failure mode of 'drilled' sample is 'shearout' while 'tailor woven' sample exhibits bearing (B1I) failure mode. And the deformation of the hole show good agreement as well.

The 3D-view videos (4 videos for 'drilled' and 'tailor woven' specimens in double and single shear tests) obtained from Micro-CT system have been uploaded as supplemental documents to provide more detailed and intuitively clear information about the specimens after failure. It proves the reliability of the FEA model and the improvement of mechanical performance due to the tailor woven printing technique.

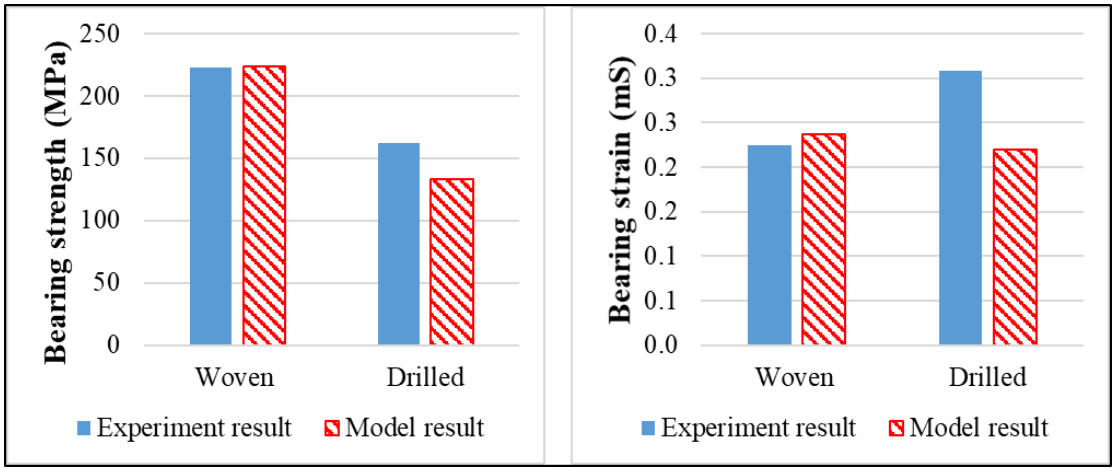

Fig. 16 Bearing strength (left) and strain (right) for 'tailor woven' and 'drilled' specimens in single shear loading test

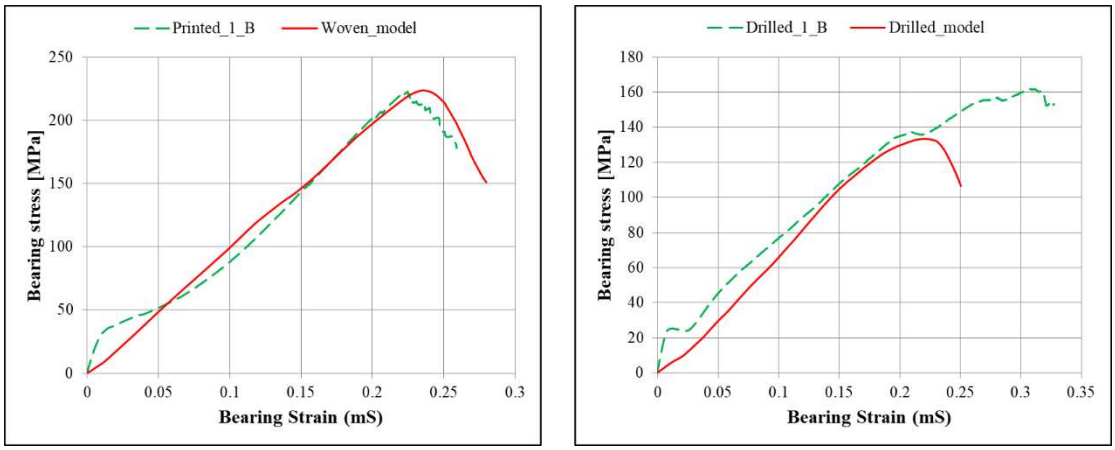

Fig. 17 Stress-strain curves for 'tailor woven' (left) and 'drilled' (right) specimens in single shear loading test

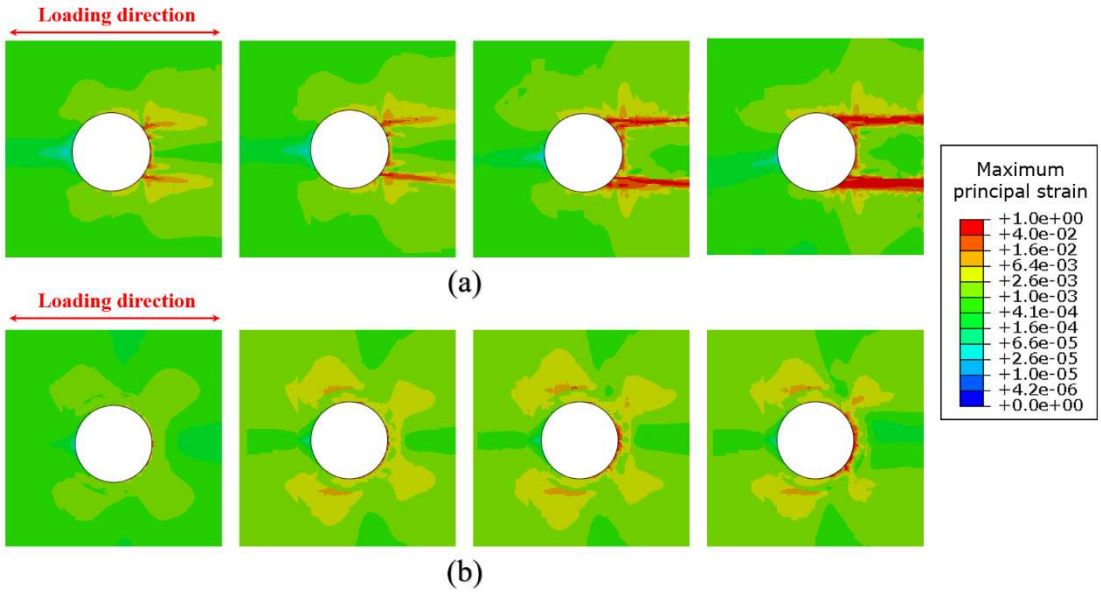

Fig. 18 Progressive distribution of maximum principal strains in single shear loading test: (a) 'drilled' and (b) 'tailor woven' specimens

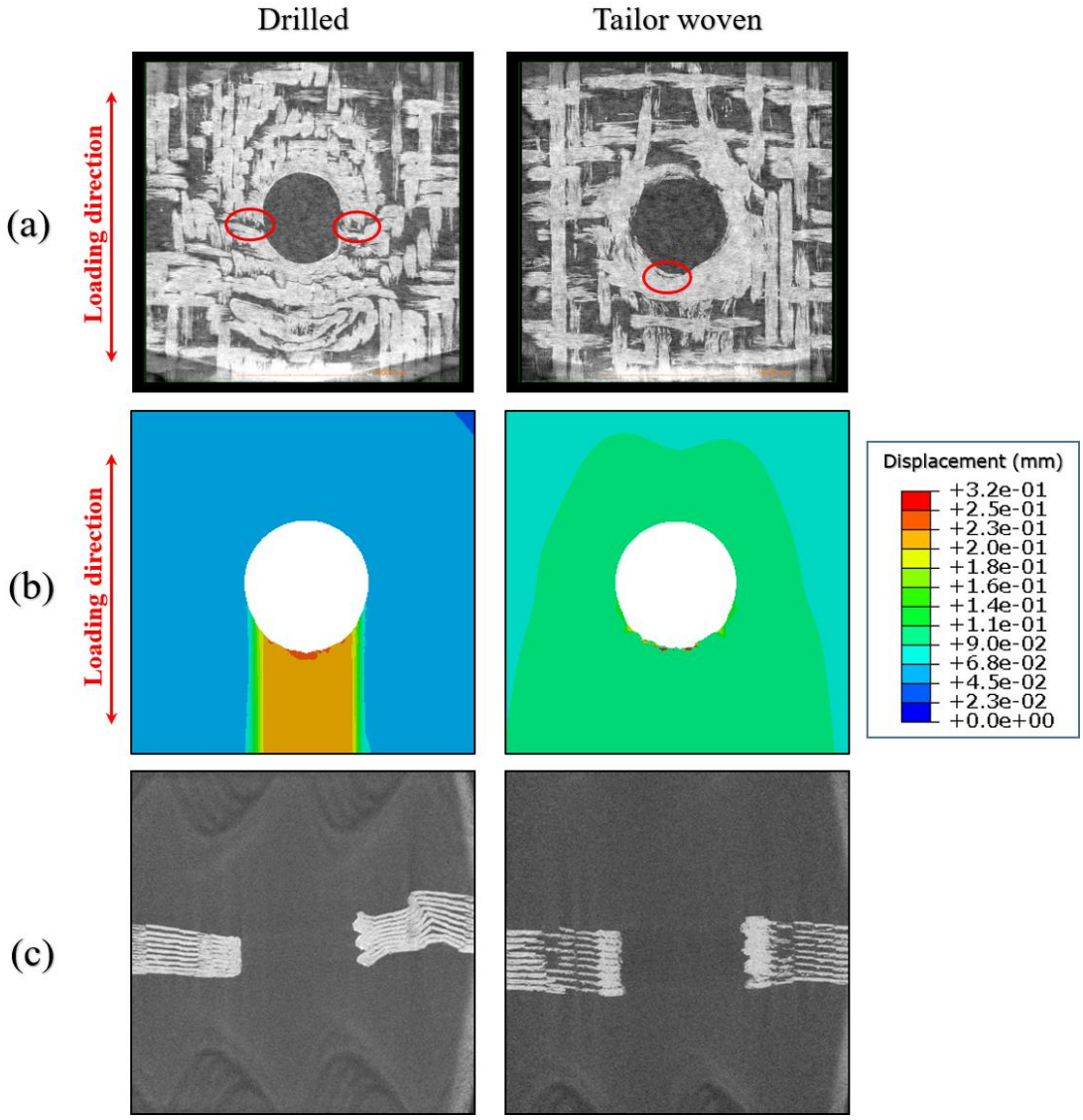

Fig. 19 (a) Cross section images after failure from Micro CT scanning (b) The distribution of displacement after failure (c) Vertical section images after failure from Micro CT scanning: 'drilled' (left) and 'tailor woven' (right) specimen in signle shear loading test

5. Conclusions

This paper presents the FE modelling and failure analysis of 3D printed woven composite plates into which 6 mm holes were placed. The specimens were obtained using the 'tailor woven' and 'drilled' techniques by diverting the filament to make the hole during printing and by drilling the hole respectively. The models of each specimen are established by FEM and Hashin failure criteria is used to predict the damage

initiation and evolution of 3D printed woven carbon fibre reinforced polymer composites. Three mechanical tests, tensile and double-and single shear loading, are studied. Also Digital Image Correlation (DIC) and Micro X-ray computed tomography (Micro-CT) scanning were used to characterise the failure process. The numerical and experimental results show good correlation. Using tailor woven printing technique, the avoidance of fibre breakage and the overlap of printed materials around the hole have dramatically increased the strength of the woven laminates. This also improved the damage process in these three loading cases in terms of the migration of the damage initiation and prevention of cracks propagation.

The FE model itself could offer a useful tool for analysing the mechanical performance of 3D printed composites with designed fibre placement. The failure analysis in this paper clarify the mechanism behind the improvement of performance achieved by tailor woven fibre placement, which can be used for the design of future 3D printing process for FRP composites. It is important to highlight that while the mechanical properties are improved, the relationship between performance and fibre placement has not been quantified. Also the performance of 3D printed woven composites under complex loading and geometry have not been tested. Future research is required to address these issues.

6. Acknowledgements

This research was supported by Irish Manufacturing Research and SFI through the I-Form Advanced Manufacturing Research Centre 16/RC/3872, and EPSRC National Centre for Infrastructure Materials EP/P017169/1.

Reference

[1] Zhan X, Meng Y, Zhou J, Qi C, Zhang C, Gu D. Quantitative research on microstructure and thermal physical mechanism in laser melting deposition for Invar alloy. Journal of Manufacturing Processes. 2018;31:221-31.

[2] Li J, Su M, Wang X, Liu Q, Liu K. Laser deposition-additive manufacturing of ceramics/nanocrystalline intermetallics reinforced microlaminates. Optics & Laser Technology. 2019;117:158-64.

[3] Parandoush P, Lin DJCS. A review on additive manufacturing of polymer-fiber composites. 2017;182:36-53.

[4] Jenett B, Calisch S, Cellucci D, Cramer N, Gershenfeld N, Swei S, et al. Digital Morphing Wing: Active Wing Shaping Concept Using Composite Lattice-Based Cellular Structures. Soft Robot. 2017;4(1):33-48.

[5] Esposito Corcione C, Gervaso F, Scalera F, Montagna F, Sannino A, Maffezzoli A. The feasibility of printing polylactic acid-nanohydroxyapatite composites using a low-cost fused deposition modeling 3D printer. Journal of Applied Polymer Science. 2017;134(13).

[6] Dudek P. FDM 3D Printing Technology in Manufacturing Composite Elements. Archives of Metallurgy and Materials. 2013;58(4).

[7] Khashaba UA, Sebaey TA, Selmy AI. Experimental verification of a progressive damage model for composite pinned-joints with different clearances. International Journal of Mechanical Sciences. 2019;152:481-91.

[8] Blok LG, Longana ML, Yu H, Woods BKS. An investigation into 3D printing of fibre reinforced thermoplastic composites. Additive Manufacturing. 2018;22:176-86.

[9] Caminero M, Chacón J, García-Moreno I, Reverte J. Interlaminar bonding performance of 3D printed continuous fibre reinforced thermoplastic composites using fused deposition modelling. Polymer Testing. 2018;68:415-23.

[10] Caminero M, Chacón J, García-Moreno I, Rodríguez G. Impact damage resistance of 3D printed continuous fibre reinforced thermoplastic composites using fused deposition modelling. Composites Part B: Engineering. 2018;148:93-103.

[11] Justo J, Távara L, García-Guzmán L, París F. Characterization of 3D printed long fibre reinforced composites. Composite Structures. 2017.

[12] Al Abadi H, Thai H-T, Paton-Cole V, Patel VI. Elastic properties of 3D printed fibre-reinforced structures. Composite Structures. 2018;193:8-18.

[13] Dickson AN, Barry JN, McDonnell KA, Dowling DP. Fabrication of continuous carbon, glass and Kevlar fibre reinforced polymer composites using additive manufacturing. Additive Manufacturing. 2017;16:146-52.

[14] Zhang H, Yang D, Sheng Y. Performance-driven 3D printing of continuous curved carbon fibre reinforced polymer composites: A preliminary numerical study. Composites Part B: Engineering. 2018;151:256-64.

[15] Malakhov AV, Polilov AN. Design of composite structures reinforced curvilinear fibres using FEM. Composites Part A: Applied Science and Manufacturing. 2016;87:23-8.

[16] Passos AG, Luersen MA, Steeves CA. Optimal curved fibre orientations of a composite panel with cutout for improved buckling load using the Efficient Global Optimization algorithm. Engineering Optimization. 2016;49(8):1354-72.

[17] Yamanaka Y, Todoroki A, Ueda M, Hirano Y, Matsuzaki R. Fiber Line Optimization in Single Ply for 3D Printed Composites. Open Journal of Composite Materials. 2016;06(04):121-31.

[18] Koricho EG, Khomenko A, Fristedt T, Haq M. Innovative tailored fiber placement technique for enhanced damage resistance in notched composite laminate. Composite Structures. 2015;120:378-85.
[19] Uhlig K, Tosch M, Bittrich L, Leipprand A, Dey S, Spickenheuer A, et al. Meso-scaled finite element analysis of fiber reinforced plastics made by Tailored Fiber Placement. Composite Structures. 2016;143:53-62.
[20] Crothers P, Drechsler K, Feltin D, Herszberg I, Kruckenberg T. Tailored fibre placement to minimise stress concentrations. Composites Part A: Applied Science and Manufacturing. 1997;28(7):619-25.
[21] Dickson AN, Ross K-A, Dowling DP. Additive manufacturing of woven carbon fibre polymer composites. Composite Structures. 2018;206:637-43.
[22] Dickson AN, Dowling DP. Enhancing the bearing strength of woven carbon fibre thermoplastic composites through additive manufacturing. Composite Structures. 2019;212:381-8.
[23] O'Connor HJ, Dowling DP. Low‐pressure additive manufacturing of continuous fiber‐reinforced polymer composites. Polymer Composites. 2019;40(11):4329-39.
[24] Mei Z, Chung D. Thermal history of carbon-fiber polymer-matrix composite, evaluated by electrical resistance measurement. Thermochimica acta. 2001;369(1-2):87-93.
[25] Hashin Z, Rotem A. A Fatigue Failure Criterion for Fiber Reinforced Materials. Journal of Composite Materials. 1973;7(4):448-64.
[26] Hashin ZJJoam. Failure criteria for unidirectional fiber composites. 1980;47(2):329-34.
[27] Nunes F, Silvestre N, Correia JR. Structural behaviour of hybrid FRP pultruded columns. Part 2: Numerical study. Composite Structures. 2016;139:304-19.
[28] Duarte A, Sáez AD, Silvestre N. Comparative study between XFEM and Hashin damage criterion applied to failure of composites. Thin-Walled Structures. 2017;115:277-88.
[29] R. Koloor SS, Khosravani MR, Hamzah RIR, Tamin MN. FE model-based construction and progressive damage processes of FRP composite laminates with different manufacturing processes. International Journal of Mechanical Sciences. 2018;141:223-35.
[30] Markforged I. Markforged materials datasheet. 2016.
[31] Jin N, Wang F, Wang Y, Zhang B, Cheng H, Zhang H. Failure and energy absorption characteristics of four lattice structures under dynamic loading. Materials & Design. 2019;169.
[32] Pinho ST, Robinson P, Iannucci L. Fracture toughness of the tensile and compressive fibre failure modes in laminated composites. Composites science and technology. 2006;66(13):2069-79.
[33] Xu J, Li C, Mi S, An Q, Chen M. Study of drilling-induced defects for CFRP composites using new criteria. Composite Structures. 2018;201:1076-87.
[34] Setoodeh S, Abdalla MM, Gürdal Z. Design of variable–stiffness laminates using lamination parameters. Composites Part B: Engineering. 2006;37(4-5):301-9.
[35] Huang J, Haftka RT. Optimization of fiber orientations near a hole for increased load-carrying capacity of composite laminates. Structural and Multidisciplinary Optimization. 2005;30(5):335-41.